Journal of Applied Polymer Science

Preparation and characterization of poly(vinyl alcohol) biocomposites with microalgae ash

Dang Thuan Tran,[1] Hyun Ro Lee,[2] Simon Jung,[3] Min S. Park,[1] Ji Won Yang,[2] Yong Keun Chang[1,2]

[1]Advanced Biomass R&D Center, KAIST 291, Daehak-ro, Yuseong-gu, Daejeon 34141, Republic of Korea

[2]Department of Chemical and Biomolecular Engineering, KAIST 291, Daehak-ro, Yuseong-gu, Daejeon 34141, Republic of Korea

[3]Korea Research Institute of Chemical Technology, 141 Gajeongro, Yuseong, Daejeon 305-600, Republic of Korea

Correspondence to: D. T. Tran (E-mail: tdangthuan@gail.com or tdangthuan@kaist.ac.kr)

ABSTRACT: Gasification of microalgae feedstock generates mineral ash. In this work, raw ash is produced from lipid-extracted algal biomass of the *Nannochloropsis salina* strain. Prior to using it as filler for composite fabrication with poly(vinyl alcohol), raw ash (RASH) is activated with NaOH and surface modified with (3-aminopropyl)triethoxysilane. Surface modification of activated ash (PASH) significantly improves interfacial interaction between surface-modified ash (GASH) and polymer matrix. Higher ultimate tensile strength of PVA/GASH composites is recorded, compared with PVA/RASH and PVA/PASH. Young's modulus of biocomposites appears to increase proportionally to loading of the fillers. Thermal properties of polymeric materials of PVA with these ashes are stable. This is the first report to demonstrate the utilization of microalgal ash, the leftover after completed gasification of algal biomass, as an efficient filler for production of value-added polymeric materials. It is proposed that microalgal ash is capable of improving the economic feasibility of microalgae-based biorefinery. © 2016 Wiley Periodicals, Inc. J. Appl. Polym. Sci. **2016**, *133*, 43599.

KEYWORDS: composites; mechanical properties; thermal properties

Received 13 November 2015; accepted 4 March 2016
DOI: 10.1002/app.43599

INTRODUCTION

In terms of thermal and biochemical conversions, microalgae is a promising renewable feedstock to produce fuels, chemicals, and high-value products.[1,2] The lipid-extracted microalgal biomass (LEA) can effectively be utilized to improve the economic feasibility of microalgae-based biodiesel production.[3] This can be accomplished by valorization of microalgal biomass to produce value-added products such as biocomposite materials. In this work, fly ash (FA) of microalgal biomass is used for synthesis of biocomposites, in conjunction with the successful microalgal biorefinery operations.

Huge quantities of FA have been mainly generated from the coal-fired power plant and accordingly, scientific research on characterization and utilization of FA as the reinforcement materials for composite synthesis has been carried out for the past decade.[4] A wide range of the polymeric matrices have been used for incorporation with FA in composite fabrication, while those, such as polyester,[5] epoxy,[6] and polypropylene (PP),[7] high density polyethylene (HDPE),[8] etc. are mainly thermoplastics synthesized via petroleum-based routes.

Due to relatively high strength and easy control of thermal processing, petroleum-based polymers have been popular over the past century. However, their composites with FA indicated low mechanical properties. When FA was incorporated into polymeric matrices at high loading, there was a significant loss in tensile strength. It was caused by weak interfacial interaction and adhesion between polymer matrices and FA surfaces. In addition, as most of the conventional petroleum-based polymers are nonbiodegradable, their increasing accumulation in the environment has been harmful and hazardous to the environment and mankind.[9]

In recent years, poly(vinyl alcohol) (PVA) has been attractive for many commercial applications as it has relatively high tensile strength, biodegradability, and water solubility. Thus, PVA are fabricated for wide range of composite synthesis using both inorganic materials, e.g., hydroxyapatite (HA),[10] multi-walled carbon nanotubes,[11] graphene oxide (GO),[12] graphene nanosheets (GNSs),[13] conductive fillers (carbon black and aluminium),[14] and intercalated montmorillonite (MMT),[15] and organic materials, e.g., agrowastes,[16] macroalgal,[17] and cellulose nanofibrils.[18]

PVA and its composites are used in a variety of applications particularly for medical and pharmaceutical industry, such as wound dressing,[19] artilage, and orthopedic.[20] They are also used as mulch film in agriculture[21,22] and as packaging film in the

food industry. Other industries have been using PVA and PVA composites for fiber, textile for sizing, finishing, coating, adhesives, emulsifiers, and colloidal stabilizers.[23] The effects of several modification methods and levels of filler loading on tensile strength of composite materials have been investigated. Thus, many studies were conducted, more focusing on fabrication of raw FA,[4] chemically modified FA,[24] and mechanically-modified FA with the addition of glutaraldehyde as a traditional cross-linking agent.[25,26] From these studies, morphological and polymer–filler interfacial interaction at high loading, for instance 25%, were not clearly elucidated.

In this work, in order to maximizing the economic benefit of microalgal-derived FA, raw FA obtained from lipid-extracted algal biomass (LEA) of the microalgal strain, i.e., *Nannochloropsis salina,* has undergone hydrothermal-chemical treatment with NaOH 1N at 100 °C. Then, the activated FA was surface-functionalized with 3-aminopropyl triethoxysilane (APTES) to produce APTES-grafted FA. These raw, activated and surface-modified FAs were used as fillers for PVA biocomposite synthesis. The composite films were synthesized by using solution casting method. Chemical composition, surface area, morphology, particle size, and crystal structures of raw FA, activated FA, and surface modified FA were characterized by using X-ray fluorescence (XRF), Brunauer–Emmett–Teller (BET) system, scanning electron microscope (SEM), dynamic light scattering (DLS), and X-ray diffractometer (XRD). Mechanical and thermal properties of PVA biocomposites were analyzed using universal testing machine (UTM) and differential scanning calorimeter (DSC). Interfacial interaction between PVA matrices and the loaded fillers were analyzed by observing morphological behavior using scanning electron microscope (SEM) and Fourier transform infrared spectroscopy (FT-IR).

EXPERIMENTAL

Materials

Poly(vinyl alcohol) with molecular weight of M_W = 89,000–98,000 g/mol (99+% hydrolyzed) and (3-aminopropyl)triethoxysilane (APTES) (99%) were purchased from Sigma-Aldrich (St. Louis, MO, USA). Microalgal biomass of the strain *Nannochloropsis salina* was supplied by NLP (Busan, Republic of Korea). This biomass was applied for the lipid extraction process, which employs hexane as solvent and 10% H_2SO_4 at 120 °C and 150 rpm in a 500 L stainless steel high pressure reactor. The reacted mixture was filtered to obtain the liquid phase containing lipids, and the separated slurry phase containing LEA. The slurry was further centrifuged at 10,000 rpm to remove solvent and acid, which enables to separate decanted LEA. The condensed LEA was dried in an oven at 105 °C until constant weight is obtained. Then it was ground into micrometer-size powder using a grinder (hmf-995, Hanil Science Industrial, Incheon, Republic of Korea). A muffle furnace (CRF M30P, ILSINTECH, Daejeon, Republic of Korea) heated up the micro-sized LEA powder in the air at 575 °C for 3 h to produce raw ash, which was designated as RASH. This RASH went through hydrothermal–chemical pretreatment step in NaOH 1N solution (10 g RASH/60 mL NaOH) at 110 °C for 1 h. The mixture was filtered with Whatman® filter paper grade 1 and washed with de-ionized water until pH 7 is obtained. The filtrate was dried at 105 °C for 24 h to obtain activated ash. The activated ash was designated as PASH.

Surface Modification of Activated Ash

The PASH particles were surface modified with 3-aminopropyl triethoxysilane (APTES). Prior to surface modification, 20 mL of APTES was mixed with 100 mL water–methanol solution (water:methanol vol. ratio = 3:1) at room temperature and stirred at 400 rpm for 30 min to fully hydrolyze the silane species. Surface modification was then accomplished by adding 8 g of PASH into the hydrolyzed APTES solution under vigorous stirring, followed by sonication with ultrasonic device (5510R-DTH, Branson Ultrasonics, Danbury, USA) for 10 min. After sonication, the suspension was stirred at 400 rpm and 40 °C for 2 h. This heterogeneous mixture was filtered with Whatman® filter paper grade 1 and washed with 1 L deionized water. Then it went through 100 mL of pure ethanol to completely remove free APTES. It was finally dried in an oven at 105 °C for 24 h to result in surface-modified ash, which then was designated as GASH.

Preparation of Composite Materials

Composite materials were prepared by using solution casting method. The RASH, PASH, and GASH were added to a 250 mL beaker containing water as solution under vigorous stirring at 400 rpm for 5 min. It was sonicated by an ultrasonic device (5510R-DTH, Branson Ultrasonics, Danbury, USA) for 10 min. PVA was added to the suspension and kept stirring at 400 rpm for 5 min to well disperse PVA particles in the suspension. The content of reinforcement materials varied at 5, 10, 15, 20, and 25 wt % of PVA biocomposites, while the solid content over total volume of solution kept constant at 12% (w/v). After the PVA–ash–water mixture was heated at 90 °C under stirring at 350 rpm for 1 h, the heterogeneous solution was then casted on a flat glass plate supported by a knife coating device (KP-3000, KEEPAE, Suwon, Republic of Korea). Accordingly, the doctor blade (IMOTO 1117/150, KEEPAE, Suwon, Republic of Korea) produced the casting, which then was dried under ambient temperature to obtain thin film with consistent thickness.

Characterizations of RASH, PASH, and GASH

Chemical composition of RASH, PASH, and GASH were determined by X-ray fluorescence (XRF) (ZSX Primus III+, Rigaku, Tokyo, Japan). The surface areas of the RASH, PASH, and GASH were determined by BET analysis using an AUTOSORB-1 analyzer (Quantachrome Corporation, Boynton Beach, FL). Dynamic Light Scattering (DLS) (Zetasizer Nano ZS90, Malvern Instruments, Worcestershire, UK) was used to determine particle size distribution and average particle size of RASH, PASH, and GASH, which were dispersed in deionized water by ultrasonic device (5510R-DTH, Branson Ultrasonics, Danbury).

X-ray Diffraction (XRD)

Diffraction patterns of RASH, PASH, and GASH were recorded by a high-resolution powder X-ray diffractometer (SmartLab, Rigaku, Tokyo, Japan) using Cu K_α radiation (λ = 1.5406 Å) at 2Theta from 5° to 90°, scan speed 5°/min and step size 0.02°, power 45 kV and 200 mA. The biocomposite films were characterized by Multi-Purpose Thin-film X-ray Diffractometer (D/

MAX-2500, Rigaku, Tokyo, Japan) at 2Theta from 5° to 90°, scan speed 5°/min and step size 0.02°, power 45 kV and 200 mA. Average crystallite size was calculated from full width at half maximum (FWHM) of the XRD peak using Scherrer's equation:

$$L = \frac{K\lambda}{\beta(2\theta)\cos\theta} \quad (1)$$

where $\beta(2\theta)$ is the full width at half maximum (FWHM), K is a constant taken as the normal value of 0.94, λ is the wavelength of X-ray wavelength (for copper, λ = 1.5406 Å), and θ is the Bragg angle.[25,27] The peak at around 19.3° was used to estimate average crystallite size.

Fourier Transform Infrared Spectroscopy (FT-IR)

IR spectra of ash powders and the composite films were recorded on a FT-IR (Alpha, Bruker, Billerica) run with OPUS software. The conditions for FT-IR measurements were scan range from 4000 to 400 cm^{-1} with 24 scans, and resolution of 4 cm^{-1}.

Scanning Electron Microscopy (SEM)

The morphology of RASH, PASH, and GASH as well as the composite films were examined using scanning electron microscopy (SEM, Hitachi S-4800) at an acceleration voltage of 10 kV after about 3 nm-thick platinum coatings.

Differential Scanning Calorimetry (DSC)

DSC analysis was performed on an Ultra-Low Temperature Differential Scanning Calorimetry (DSC 214 Polyma, Netzsch, Selb/Bavaria, Germany) under nitrogen flow at 20 mL/min flow rate. Sample weight between 2.39 and 4.91 mg were hermetically sealed in an aluminum DSC pan and placed in the DSC cell. The DSC scan was calibrated with indium as a standard. Samples were first heated from 0 to 100 °C and cooled from 100 to 0 °C at the rate of 10 °C/min. In the second cycle, samples were heated from 0 to 250 °C at the rate of 10 °C/min, and heat flow (W/g) was measured with temperature variations. The % crystallinity (X_C) of the samples was calculated using following equations.[25,27–29]

$$X_C = \frac{\Delta H_f}{W_i \times \Delta H_f^*} \quad (2)$$

where ΔH_f^* is the enthalpy of melting of PVA with 100% crystallinity having a value of 138.60 J/g, ΔH_f is the enthalpy of fusion of the composite (J/g), and W_i is the weight fraction of the polymer in the biocomposite.[25,27]

Mechanical Testing

The specimens were stamp cut by using a metallic tool and then they were stored at 25 °C and 43% relative humidity over saturated K_2CO_3, which was in accordance with ASTM E104-02 by maintaining constant relative humidity using aqueous solutions for at least 24 h before testing. Tensile tests were carried out on an Instron Universal 5583 testing system (Instron, Norwood). According to ASTM D882-12, the specimens have a width of 10 mm and length 30 mm, of which film thickness was analyzed by averaging three measurements along the test using a digimatic indicator (ID-S112XB, Mitutoyo Corp., Kanagawa, Japan) in the range of 0.097–0.174 mm. Measurements were performed at a crosshead speed of 10 mm/min. Three specimens were made from each sample and triplicate measurements were averaged to report the final value.

Table I. Chemical Compositions of RASH, PASH, and GASH Analyzed by XRF

Component (wt %)	RASH	PASH	GASH
C	ND	3.2	3.4
B_2O_3	4.7	ND	ND
Na_2O	1.9	2.4	2.5
MgO	2.6	3	3.1
Al_2O_3	4.3	5	5.2
SiO_2	24.4	28	28.1
P_2O_5	13.2	17.1	16.6
SO_3	23.3	3.6	3.3
K_2O	2.1	1	1.1
CaO	17.6	22.2	22.4
TiO_2	0.5	0.6	0.8
MnO	0.1	0.1	0.2
Fe_2O_3	4.5	4.6	4.6
ZnO	0.5	0.6	0.7
Others	0.3	8.6	8
Surface area (m^2/g)	4.8	65.2	68.7
Average particle size (μm)	2.5 ± 0.8	2.2 ± 0.9	1.9 ± 0.8
D_{10} (μm)	1.7	1.6	1.4
D_{50} (μm)	2.3	2.1	1.7
D_{90} (μm)	3.3	2.7	2.1
Span	0.70	0.52	0.41

ND: not detected.
D_{10}, D_{50}, D_{90} presenting the size, from which 10, 50, 90% (by volume or number) of particles in the sample are smaller or greater than.
Span = $(D_{90} - D_{10})/D_{50}$.

RESULTS AND DISCUSSION

Characterizations of RASH, PASH, and GASH

Chemical compositions of RASH, PASH, and GASH are listed in Table I. XRF mainly detected SiO_2 (24.4%), CaO (17.6%), Fe_2O_3 (4.5%), Al_2O_3 (4.3%) as metal oxides, P_2O_5 (13.2%) and SO_3 (23.3%) as nonmetal oxides in RASH. In contrast, SiO_2 (27.8%), CaO (22.2%), Fe_2O_3 (4.6%), Al_2O_3 (5.0%), P_2O_5 (17.1%), and SO_3 (3.6%) were detected in PASH. Slight increase was observed in metal oxide content after hydrothermal treatment using NaOH, while proportion of nonmetal oxide SO_3 decreased significantly. This change occurs due to formation of structurally new crystalline phase in PASH, which is confirmed by new crystalline peaks in XRD spectrum of PASH as shown in Figure 1. According to Table I, the portion of SiO_2 in GASH was measured as 28.1%, which is a slight increase compared to that of PASH. This slight increase was caused by the deposition of silane specie on the surface of PASH hydrolyzed from ATPES

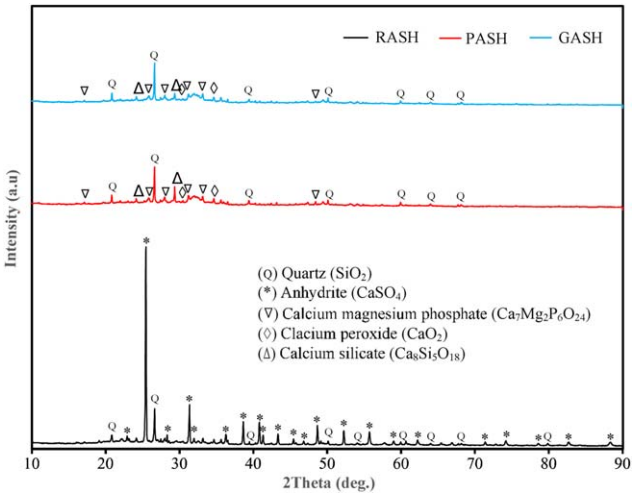

Figure 1. XRD pattern of RASH, PASH, and GASH. (Q) Quartz (SiO_2), (*) anhydrite ($CaSO_4$), (∇) calcium magnesium phosphate ($Ca_7Mg_2P_6O_{24}$), (¤) calcium peroxide–CaO_2, (Δ) calcium silicate ($Ca_8Si_5O_{18}$). [Color figure can be viewed in the online issue, which is available at wileyonlinelibrary.com.]

during grafting process. The BET surface area of RASH, PASH, and GASH were estimated as 4.8, 65.2, and 68.7 m^2/g, respectively.

The mineralogical structures of RASH, PASH, and GASH were ascertained by high-resolution powder X-ray diffractometer (SmartLab, Rigaku, Tokyo, Japan). The spectra were analyzed by comparing with standard authentic references in MDI Jade and references. Peak matching was conducted using SQX calculation, based on chemical composition of samples. As Figure 1 presents, the spectra indicate that RASH is mainly composed of hexagonal quartz (silicon dioxide, SiO_2) and anhydrite ($CaSO_4$) as crystalline ingredients. After hydrothermal–chemical treatment with NaOH, calcium magnesium phosphate ($Ca_7Mg_2P_6O_{24}$), calcium peroxide (CaO_2), and calcium silicate ($Ca_8Si_5O_{18}$) appear as new crystal components in PASH, while anhydrite ($CaSO_4$) disappears. This new crystal structure was formed by chemical reactions with sodium hydroxide. PASH mainly contains quartz (SiO_2). GASH was generated after grafting APTES on the surface of PASH. However, it had crystal structure unchanged, compared to PASH (Figure 1).

Figure 2 presents the FT-IR spectra of RASH, PASH, and GASH, while the selected band positions are summarized in Table II. FT-IR spectrum of RASH shows seven characteristics stretching vibration bands at 460, 552, 594, 674, 799, and 1088 cm^{-1}. After hydrothermal pretreatment, appearance of broad bands was observed at 3405 and 3404 cm^{-1} and they can be caused by an asymmetrical stretching of hydroxyl O—H linked to Na^+ and/or Al^{3+} available on the surface of PASH and GASH.[30–32] The weak peak at 1636 cm^{-1} in PASH appears due to the formation of Si^{4+} in silicate (calcium silicate, $Ca_8Si_5O_{18}$) synthesis during RASH–NaOH interaction.[31] The stretching vibrations of Si—O—Al bond occur mainly from 1200 to 600 cm^{-1}.[24,30] The strong and broad band at 1088 cm^{-1} reveals the presence of crystalline ingredients in RASH, which can be related to v3 (Si—O and Si—O—Al) asymmetric stretching vibrations.[24,33] They get transformed to broader but deeper bands at 1028 and 1026 cm^{-1} in PASH and GASH during treatment steps.

Appearance of weaker bands in between 800 and 400 cm^{-1}, (viz., 799, 674, 611, 594, 552, and 460 cm^{-1} in RASH; 798, 603, 653, 447 cm^{-1} in PASH; and 797, 603, 563, and 446 cm^{-1} in GASH) reveals formation of relative larger interparticle pores.[31] It is noted that there is a shift of these bands to the lower frequencies and also increase in intensities during pretreatment. This is attributed to a decrease in amorphous silicates and corresponding increase in the crystalline silicates, which is confirmed by XRD spectra as shown in Figure 1.[31] The variations in frequencies also agree with the change in mineralogy and morphology of PASH and GASH as presented in Figure 3.

According to data shown in Figure 2, newly formed weak band appears at 1418 cm^{-1} in PASH, which are mostly indicative of C—O and/or C—H bonds available in carbonates.[31] This bonds are accountable for impurities, as the existence of C shown in PASH composition after pretreatment, listed in Table I. There is a slight shift to sharp bands at 1427 cm^{-1} and a newly form band at 1469 cm^{-1} in GASH, which is caused by C—H bonds of propyl groups of APTES anchored on the surface of PASH during grafting. In GASH, the presence of new peaks at 2928 and 2866 cm^{-1} also indicate the anchored propyl groups by C—H stretching vibrations.[34,35] The two broad bands at 3368 and 1642 cm^{-1} can be ascribed to the N—H stretching vibrations and N—H bending mode of NH_2 group.[35]

The effects of alkali hydrothermal pretreatment and surface modification on the morphology of RASH, PASH, and GASH

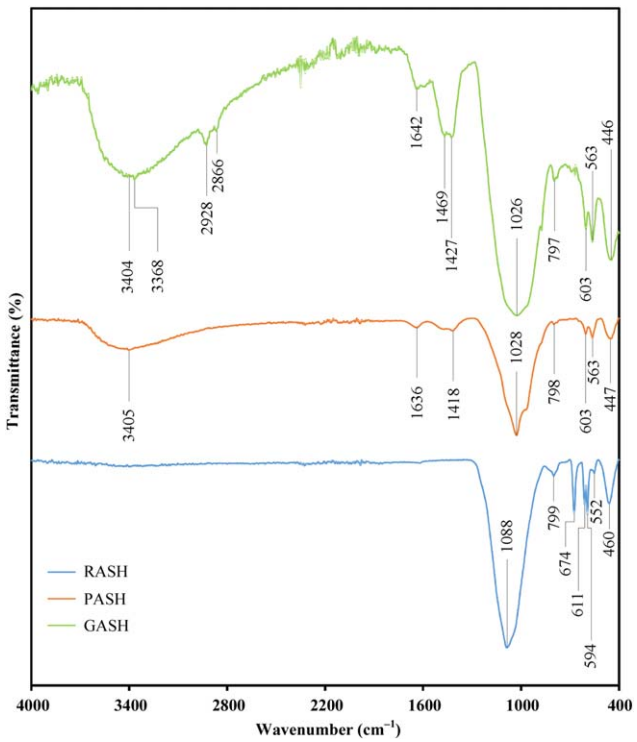

Figure 2. FT-IR spectra of RASH, PASH, and GASH. [Color figure can be viewed in the online issue, which is available at wileyonlinelibrary.com.]

Table II. Selected FT-IR Absorption Peaks of RASH, PASH, and GASH

	Peak Positions of Structural Groups at cm^{-1}							
Samples	O—H	Si—O/ Al—O	Al—O	Al—O	N—H Stretching	C—H Stretching	C—H Stretching	N—H Bending
RASH	-	1088	799	674	-	-	-	-
PASH	3405	1028	798	603	-	-	-	-
GASH	3404	1026	797	603	3368	2928	2866	1642

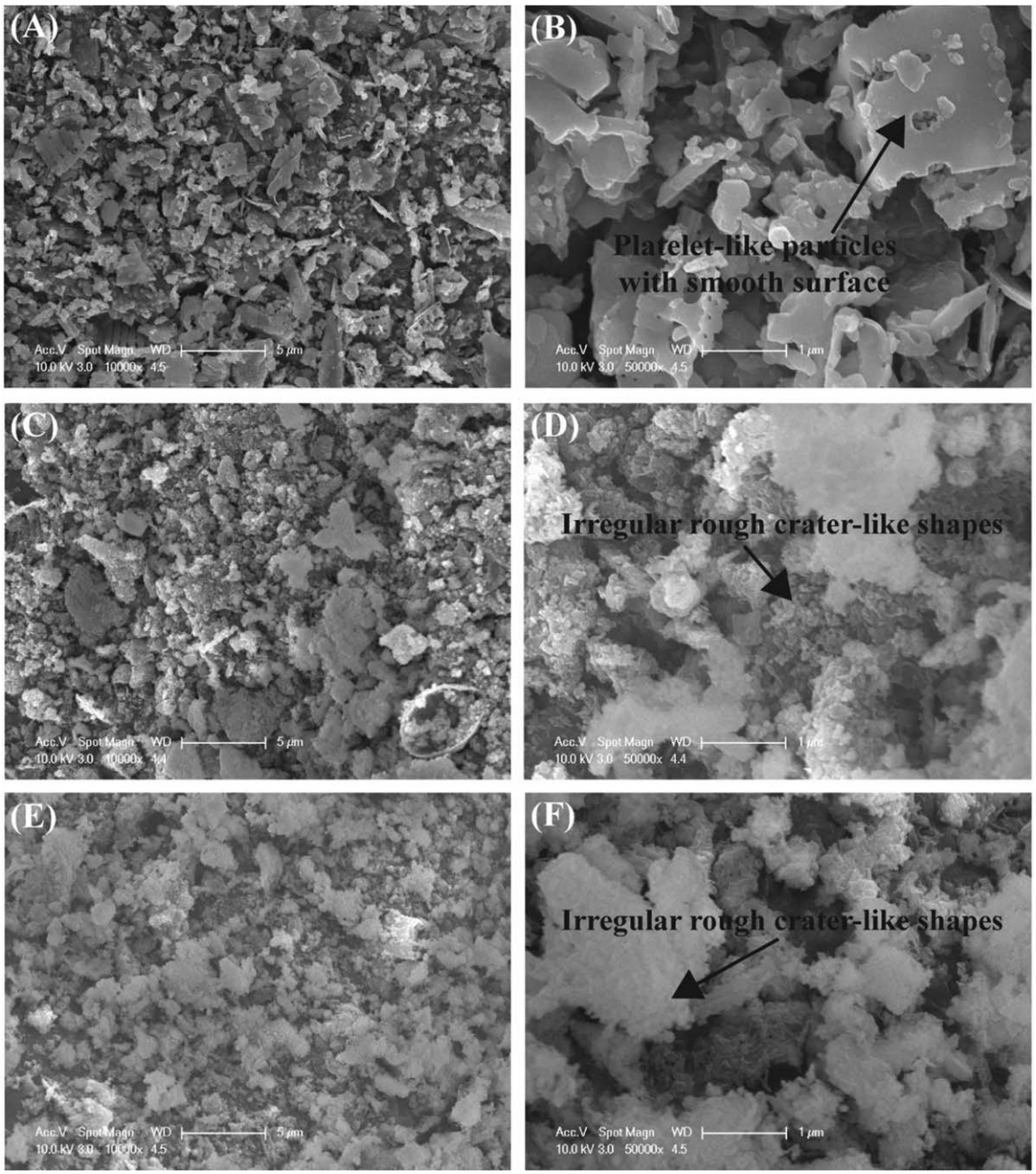

Figure 3. FE-SEM micrographs of RASH, PASH, and GASH at different magnifications: (A) RASH (×10,000) and (B) RASH (×50,000); (C) PASH (×10,000) and (D) PASH (×50,000); (E) GASH (×10,000) and (F) GASH (×50,000).

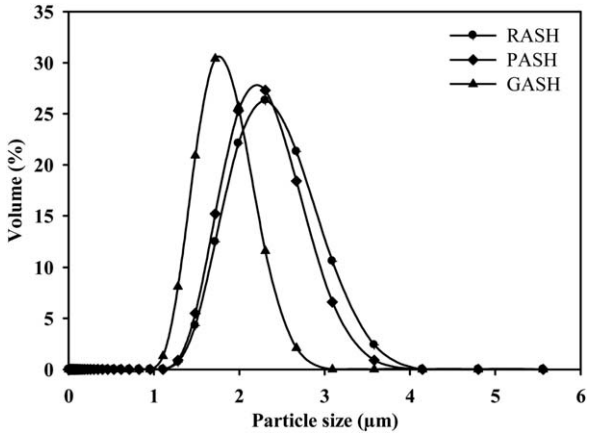

Figure 4. Particle size distributions of RASH, PASH, and GASH determined by dynamic light scattering (DLS).

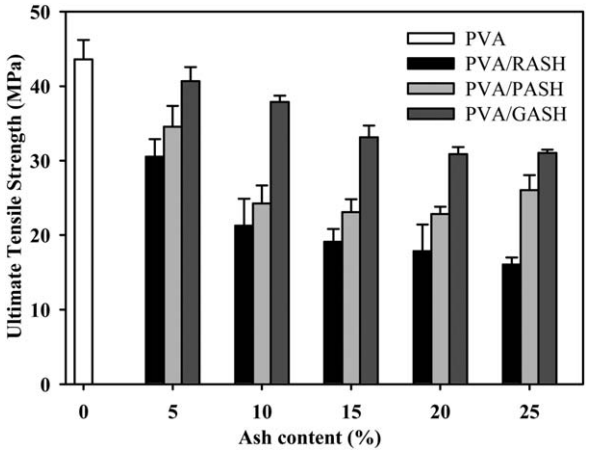

Figure 5. Ultimate tensile strength (UTS) of neat PVA, PVA/RASH, PVA/PASH, and PVA/GASH composites.

can be seen from visual analysis of SEM. Figure 3 provides SEM images of typical RASH before pretreatment, PASH after pretreatment and GASH after grafting APTES on the surface of PASH at different magnifications. Morphologies of these three types of ash particles in six images clearly indicate distinctive particles sizes and shapes. RASH indicates platelet-like particles with smooth surface [Figure 3(A,B)], whereas PASH and GASH have irregular rough crater-like shapes as shown in [Figure 3(C,D)] and [Figure 3(E,F)], respectively.

In addition, Figure 4 clearly shows a slight decrease in particle size range of PASH and GASH, compared to RASH, by shifting particle size distribution curves towards left hand side. This observation is contrastive to the data reported by Nath *et al.*[24] in which the results of increasing particle size was explained as the formation of new chemical crystalline structure and existence of high level agglomeration between particles. The average particle size of RASH is 2.3 μm at D_{50} (median size) which implies that 50% volume of the particles is less than 2.3 μm and remaining 50% is greater than 2.3 μm. Alkali hydrothermal pretreatment resulted in reduction of particles size of PASH to 2.1 μm (D_{50}), which then was further decreased to 1.7 μm in D_{50} of GASH when APTES was grafted on the surface of PASH (Table I). This implies that APTES can prevent GASH from getting agglomeration and support GASH to be well dispersed in solution. Additionally, PASH and GASH have more voids, which resulted in significantly higher surface area compared to RASH (Table I). The smaller particle size and irregular rough surfaces of PASH and GASH are important factors for increasing the interfacial interaction with polymer matrix in composite formulation.[24]

Mechanical Properties of PVA Biocomposites

The variations in ultimate tensile strength (UTS), elongation at break (EB), and Young's modulus (YM), of PVA biocomposites with RASH, PASH, and GASH are presented in Figures 5−7. The major factor for enhancement of tensile strength is interfacial interaction between the reinforcement materials and polymer matrix, which facilitates stress transfer from matrix to the filler. When filler loading increased from 5 to 25%, compared with UTS of neat PVA, there was a significant decrease in UTS value of PVA/RASH and PVA/PASH composites. With 5% of GASH loading, UTS value of PVA/GASH composites was determined as 40.7 MPa, which is comparable to 43.6 MPa of neat PVA. This UTS value of PVA/GASH composites gradually decreased, when filler loading increased from 5 to 25% as illustrated in Figure 5. The decrease of tensile strength at higher reinforcement loading is caused by extensive filler–filler interaction rather than filler–polymer interaction. This filler–filler interaction mainly attributes to slippage of the polymer chains over the irregular surface of ash particles.[25] There is also a possibility of supersaturation of RASH and PASH concentration, which results in reduction of the intimate contact area between RASH and PASH and PVA.[36] A similar trend is also observed for elongation at break (EB) in Figure 6, which transforms gradually from ductile to brittle fracture in biocomposites.

Due to an uneven distribution and agglomeration of the filler particles at higher loading (Figure 11), the gradual decreases in UTS of PVA/GASH composites are observed as depicted in Figure 5. This uneven distribution and agglomeration phenomena also reduces the significant number of available reinforcing particles. On the other hand, UTS values of the PVA/GASH composites are higher than those of PVA/RASH and PVA/PASH

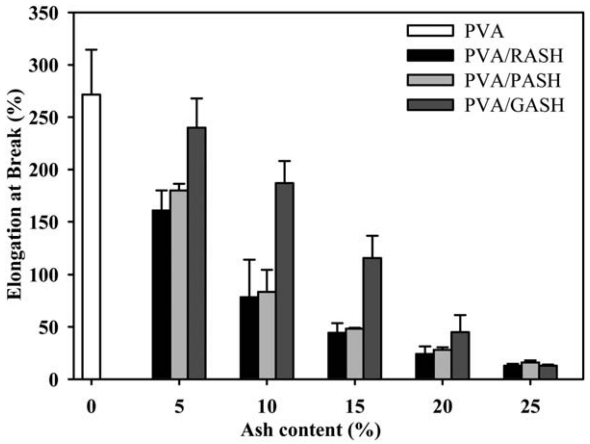

Figure 6. Elongation at break (EB) of neat PVA, PVA/RASH, PVA/PASH, and PVA/GASH composites.

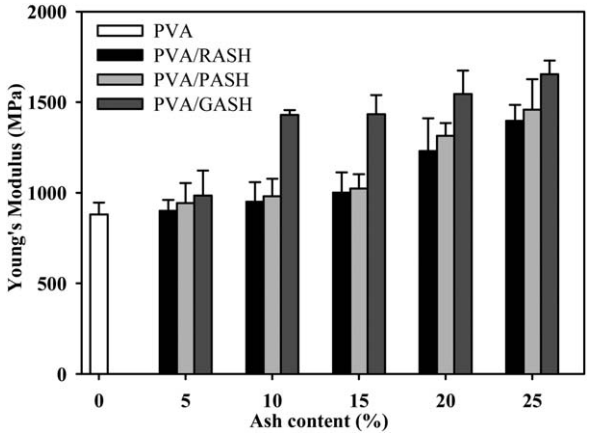

Figure 7. Young's modulus (YM) of neat PVA, PVA/RASH, PVA/PASH, and PVA/GASH composites.

composites. This attributes to the fact that there is a better dispersion of GASH in PVA matrix and existence of efficient filler–polymer interaction which was confirmed by XRD pattern in Figure 9, FT-IR spectra in Figure 10, and SEM data in Figure 11. Moreover, GASH particles are formed by functionally grafted with APTES on the surface of PASH and they have large surface area (Table I), thus when they are arranged on the nanometer scales into polymers matrix, it significantly enhances their mechanical performance.[37] The lower of UTS values of PVA/RASH composites compared to those of PVA/PASH and PVA/GASH composites is caused by larger particle size and lower surface area of RASH than PASH and GASH (Table I), which reduces interfacial interaction of RASH and PVA. In addition, the nonobvivous existence of O—H in IR spectra of RASH (Figure 2) indicated the lack of wetability of RASH, which may reduce hydrogen bonding strength which is created between RASH and PVA during composite fabrication process.

Stiffness of the filler attributes to the immobilization of polymer phase by molecular interaction as discussed by Kader *et al.*[38] This mechanism occurs through two different pathways. The first pathway is that aggregated cluster of particles breaks down in the aqueous PVA solution and the polymer phase can penetrate into the asperities on the surface of GASH. Second, the polymer chains get entrapped into the GASH, which was wrapped with APTES during the vigorous stirring and sonication processes.[25] In addition, the rough and irregular nano-sized filler particles in GASH generate uniform distribution and dispersion in PVA matrix, which results in strengthening of PVA biocomposites. Young's modulus (YM) of PVA/GASH composites increased in proportion with filler loading from 5 to 25%. In contrast, YMs of PVA/RASH and PVA/PASH composites slightly increased at loading from 5 to 15%, but then they proportionally increased at loading from 15 to 25%. As Figure 7 illustrates, YMs of PVA/GASH composites reaches about 1.7 GPa at GASH loading of 25%.

In Table III, microalgal ash polymeric materials are compared with other biocomposite examples from the literature that have a similar formulation. From this comparison, it can be seen that PVA/GASH composites exhibits increases of modulus and the decrease in elongation, similar to polymeric materials of PVA with raw fly ash (PVA/FA) formulated by Nath *et al.*[4] when filler loading increased from 5 to 10%. However, tensile strength of PVA/GASH composites decreases as GASH content increased from 5 to 10%, which is contrastive to that of PVA/FA composites in Nath *et al.*[4] Notably, tensile strength of PVA biocomposite with 5% of GASH is higher than those of PVA bioplastics with FA in Nath *et al.*,[4] FA, 30h MCA-FA and 60h MCA-FA in Patil *et al.*[25] at the same 5% filler loading. When GASH used at 10%, PVA90GASH10 exhibits tensile strength of 37.9 MPa, which is comparable to 37.4 MPa of PVA90FA10 synthesized by Nath *et al.*[4] but higher than those of all plastics of PVA with raw FA and mechanical treatment FA in Patil *et al.*[25]

PVA95RASH5 and PVA95PASH5 composites also indicates significantly higher tensile strength than all composites of PVA with 5% of FA and mechanochemically activated FA in Patil *et al.*[25] but comparable to tensile strength of PVA95FA5 in Nath *et al.*[4] In conclusion, in terms of enhancement of mechanical properties of PVA biocomposites, GASH generated by grafting of functional chemical (APTES) on the surface of PASH is more efficient than raw FA and mechanochemically activated FAs.

Table III. Comparison of Mechanical Properties of PVA/RASH, PVA/PASH, and PVA/GASH with Other PVA/FAs Biocomposites

Composite	Filler loading (%)	Ultimate tensile strength (UTS) (MPa)	Young's modulus (YM) (GPa)	Elongation at break (EB) (%)	References
PVA/FA	5	35.7 ± 2	0.14 ± NA	178 ± 5	Nath *et al.*[4]
PVA/FA	10	37.4 ± 1	0.16 ± NA	150 ± 7	Nath *et al.*[4]
PVA/FA	5	22 ± 2	1.6 ± 0.05	160 ± 10	Patil *et al.*[25]
PVA/30h MCA-FA	5	24 ± 2.5	1.65 ± 0.1	175 ± 20	Patil *et al.*[25]
PVA/60h MCA-FA	5	30 ± 2	2.4 ± 0.6	140 ± 10	Patil *et al.*[25]
PVA/RASH	5	30.6 ± 2.3	0.9 ± 0.06	160 ± 19	This study
PVA/PASH	5	34.6 ± 2.8	0.94 ± 1.1	180 ± 6.4	This study
PVA/GASH	5	40.7 ± 1.9	0.98 ± 0.14	240 ± 28	This study
PVA/GASH	10	37.9 ± 0.9	1.43 ± 0.27	187 ± 21	This study

PVA: Poly(vinyl alcohol); FA: Fly ash originated from coal-fired power plants; 30h MCA-FA: Fly ash mechanochemically activated in ball mill for 30 h; 60h MCA-FA: Fly ash mechanochemically activated in ball mill for 60 h; PASH: Microalgal-derived ash thermochemically pre-treated with NaOH 1N for 1 h; GASH: PASH grafted with (3-aminopropyl) triethoxysilane (APTES); NA: Not available.

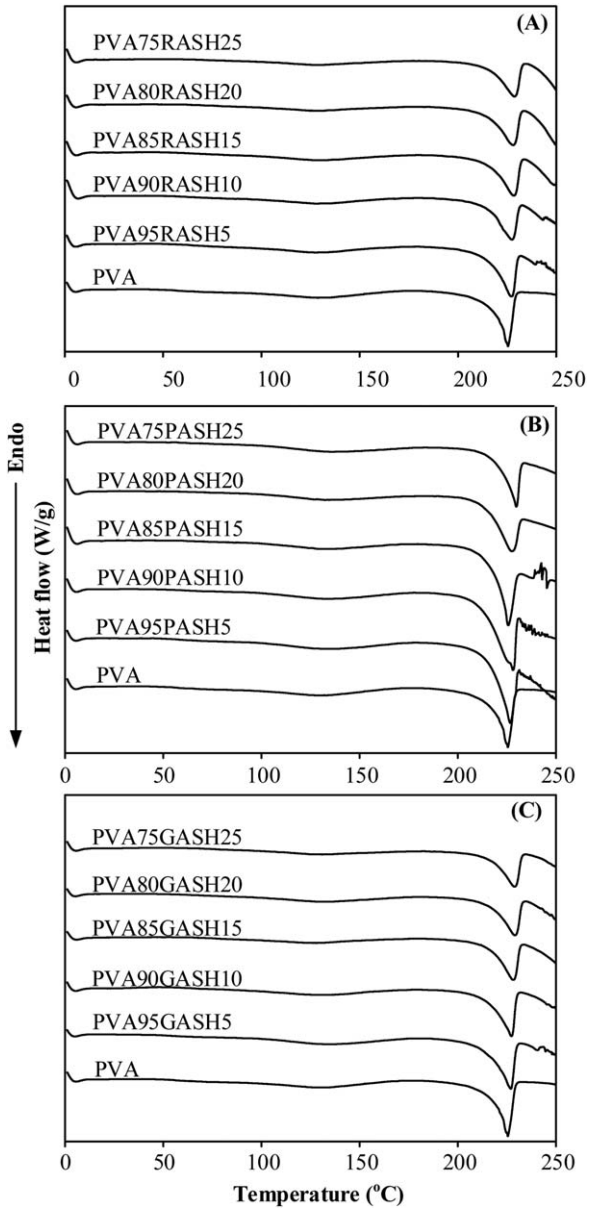

Figure 8. DSC thermograms of (A) PVA and PVA/RASH composites, (B) PVA and PVA/PASH composites, (C) PVA and PVA/GASH composites.

Thermal Properties of PVA/RASH, PVA/PASH, and PVA/GASH Biocomposites

Effect of filler concentrations on the thermal properties of PVA biocomposites were analyzed by using a differential scanning calorimeter (DSC). The first heating and cooling run of the DSC was applied to characterize thermal properties of all samples. The heating run was conducted to acquire the melting temperature and the melting enthalpy, while the cooling run was used to characterize the crystallization and fusion energy. Figure 8 presents the thermograms of neat PVA, PVA/RASH, PVA/PASH, and PVA/GASH composites at ash loading from 5 to 25%. These thermograms also indicate the second heating cycles of the samples. PVA is a semicrystalline polymer exhibiting both a glass transition temperature (T_g) and a melting endotherm (T_m) due to high physical interchain and intrachain interaction of hydroxyl groups by hydrogen bonds.[25,39]

The discontinuity at 5–10 °C is due to the glass transition of PVA. The region between 120 and 140 °C attributes to the melting of the crystallites of the crosslinked network.[27] The sharp endothermic peak in the range 220–240 °C is caused by the melting of the recrystallization of PVA.[25,27,39] The values of crystallization temperature (T_c), melting temperature (T_m), heat of melting (ΔH_m), heat of fusion (ΔH_f), and degree of crystallinity (X_c, %) of PVA biocomposite samples are summarized in Table IV.

As Table IV presents, crystallinity of pure PVA is 51.8%, which is higher than other PVA biocomposites in the range between 37.1 and 50.8% at ash loading from 5 to 25%.

Heat of fusion shows the same trend. The neat PVA has 71.8 J/g, while PVA/RASH, PVA/PASH, and PVA/GASH composites are in the range between 38.6 and 63.4 J/g. After PVA were incorporated with RASH, PASH, and GASH in the range from 5 to 25% in composite formulation, the melting temperature of PVA composites marginal changed from 225.5 to 225.6 − 229.8 °C. This is consistent with remained thermal stability with the higher initial decomposition temperature, which does not match with finding of that of hydroxyapatite (HAp)/PVA composite system.[40] The heat of melting was measured as 36.4 and 34.3 J/g for PVA95-PASH5 and PVA90PASH10, while 34.9 and 35.2 J/g for PVA95-GASH5 and PVA90GASH10, respectively. There are the slight increases, compared to 34 J/g of neat PVA. However, when PASH and GASH loading increase from 15 to 25%, the heat of melting decreases, as indicated in Table IV. The decreasing trend of heat of melting was also observed for PVA/RASH composites at 5 to 25% of RASH loading (Table IV).

XRD Analysis

Figure 9 shows XRD patterns of neat PVA, PVA/RASH, PVA/PASH, and PVA/GASH composites with filler loading increases from 5 to 25%. The sharp reflection at 2Theta angle of 19.4° is observed for neat PVA film, which is the characteristic of crystalline and amorphous phases of conventional semicrystalline polymers. XRD patterns PVA/RASH composite films at RASH loading from 2 to 25% indicated the strong peak at 2Theta of 25.4° with *d*-spacing of 0.35 nm [Figure 9(A)]. The peak attributes to the crystal structure of anhydrite ($CaSO_4$), which is commonly found in RASH as indicated in Figure 1. PVA/PASH composite films indicate the prominent crystalline peaks at 2Theta of 26.5° and 29.4° with *d*-spacing of 0.34 and 0.30 nm, respectively [Figure 9(B)]. These peaks correspond to the quarts (SiO_2) and calcium silicate ($Ca_8Si_5O_{18}$) phase of PASH (Figure 1). Figure 9(C) illustrates that PVA/GASH composites show disappearance of quartz and calcium silicate. The incorporation of APTES molecules on the surface of PASH during grafting process shows the enhanced bonding between PVA matrix and GASH surface, which leads to miss-presenting Bragg diffraction peak of GASH crystal structure [Figure 9(C)]. The incorporation of RASH, PASH, and GASH also affected the crystallite size of PVA as listed in Table V. However, due to the nucleating effect of RASH, PASH, and GASH, there is only a slight change in crystallite size.[25]

Table IV. Thermal Properties and Crystallinity of Neat PVA, PVA/RASH, PVA/PASH, and PVA/GASH Composites

Sample	T_c (°C)	T_m (°C)	ΔH_m (J/g)	ΔH_f (J/g)	Crystallinity (X_c, %)
PVA100	133.5	225.5	34.0	71.8	51.8
PVA95RASH5	133.7	227.1	30.7	52.1	39.6
PVA90RASH5	132.6	227.3	28.5	47.6	38.2
PVA85RASH15	134.8	228.3	28.8	53.2	45.5
PVA80RASH20	135.9	227.9	24.8	51.6	46.5
PVA75RASH25	135.0	228.6	24.6	49.1	47.3
PVA95PASH5	134.4	226.7	36.4	49.9	37.9
PVA90PASH10	133.1	227.9	34.3	63.4	50.8
PVA85PASH15	130.5	225.6	28.8	50.6	42.9
PVA80PASH20	132.4	227.3	28.3	43.6	39.4
PVA75PASH25	135.7	229.8	32.2	38.6	37.1
PVA95GASH5	134.1	226.9	34.9	62.6	47.5
PVA90GASH10	127.5	227.3	35.2	59.0	47.3
PVA85GASH15	128.0	228.1	25.0	47.0	39.9
PVA80GASH20	132.5	229.2	29.7	48.4	43.6
PVA75GASH25	131.1	229.0	23.4	46.4	44.7

T_c: crystallization temperature, T_m: melting temperature, ΔH_m: heat of melting, ΔH_f: heat of fusion, X_c: degree of crystallinity.

FT-IR Analysis

Figure 10 presents the FT-IR spectra of neat PVA and its composites typically containing 25% of RASH, PASH and GASH. The most of major peaks related to hydroxyl and acetate groups are observed in Figure 10. The intense peaks at 3280cm^{-1} is due to O—H stretching, arising from the intermolecular and intramolecular hydrogen bonds.[25,26] The vibrational bands at 2937 and 2910 cm^{-1} refer to C—H stretching from alkyl groups, while the band at 1655 cm^{-1} are from C=O and C—O stretchings from acetate groups in neat PVA.[4,25,26] C—H and O—H bending peaks appeared at 1417 and 1328 cm^{-1}.[26] The well-known peak at 1086 cm^{-1} is the C—O—H stretching.[4,26] The band at 839 cm^{-1} exhibits the characteristics of skeletal vibration of syndiotactic and isotactic of PVA stereosequences.[41]

In comparison with neat PVA, PVA composites with 25% RASH presented peak shifting of O—H and C—H bending to higher wave number and higher intensity, while C—O—H stretching shifted to lower wave number and higher intensity. For composite with 25% PASH, its IR spectra indicated the peak shifts of O—H, C=O, and C—O bending to the lower wave numbers and higher intensity.

This is strongly supported by intermolecular and/or intramolecular hydrogen bonding between PASH and PVA.[4,24,26] The linking of RASH and PASH with PVA and can also be supported by the following plausible hydrogen bonding between (i) C=O groups in PVA and —OH groups on the surface of RASH and PASH,[42] and (ii) —OH in PVA and Si—O groups on the surfaces of RASH and PASH.[30] For PVA75GASH25 composite, the peak shifts were observed for O—H stretching with broader and higher intensity, C=O and C—O bending with higher intensity, and C—H stretching with deeper and higher intensity to lower wave numbers. This is caused by strong intermolecular and intramolecular hydrogen bondings among not only O—H groups, but also —NH_2 groups on the surface of GASH and O—H groups in PVA matrix.

The peak at 2866 cm^{-1} in GASH shifted to 2854 cm^{-1} in PVA75GASH25 composite, which was due to the anchored propyl groups by C—H stretching vibrations. The arising new peaks at 1740 and 1709 cm^{-1} in PVA75GASH25 composite are caused by chemical reaction of functional groups on GASH in PVA matrix. The hydrogen bonding is partially linked the high modulus of ash particles. It restricted the mobility of PVA polymeric chains, which resulted in reduction of ductility under load. It also negotiated efficient load transfer between ash and PVA.[4] The chemical reactions in the composite system can be summarized as (i) reaction between —OH groups on the surface of ashes and —OH groups of PVA, and (ii) reaction between —NH_2 groups on the surface of GASH and —OH groups of PVA. Due to these reactions, strong chemical bridges were established between PVA and ash with APTES.

SEM Analysis

Morphologies of the composite materials explains nature of adhesion, failure, and mechanical properties, which were examined using SEM images of fractured cross-section films.

Figure 11 presents the presentative images of PVA composites at ash loading of 5 and 25%. Figure 11(A) shows morphologically cross-sectional area of PVA95RASH5 composite, which depicts poor-filler matrix linking due to inefficient distribution of RASH filler in PVA matrix. Cracks appeared perpendicular to the plane of composite film when loading of RASH increased to 25% as illustrated in Figure 11(B), which causes significantly falling of mechanical strength of PVA75RASH25 as revealed in Figures 5–7.

Figure 11(C) illustrates the fractured surface of the PVA95-PASH5 composites, which shows partial full coverage of PVA

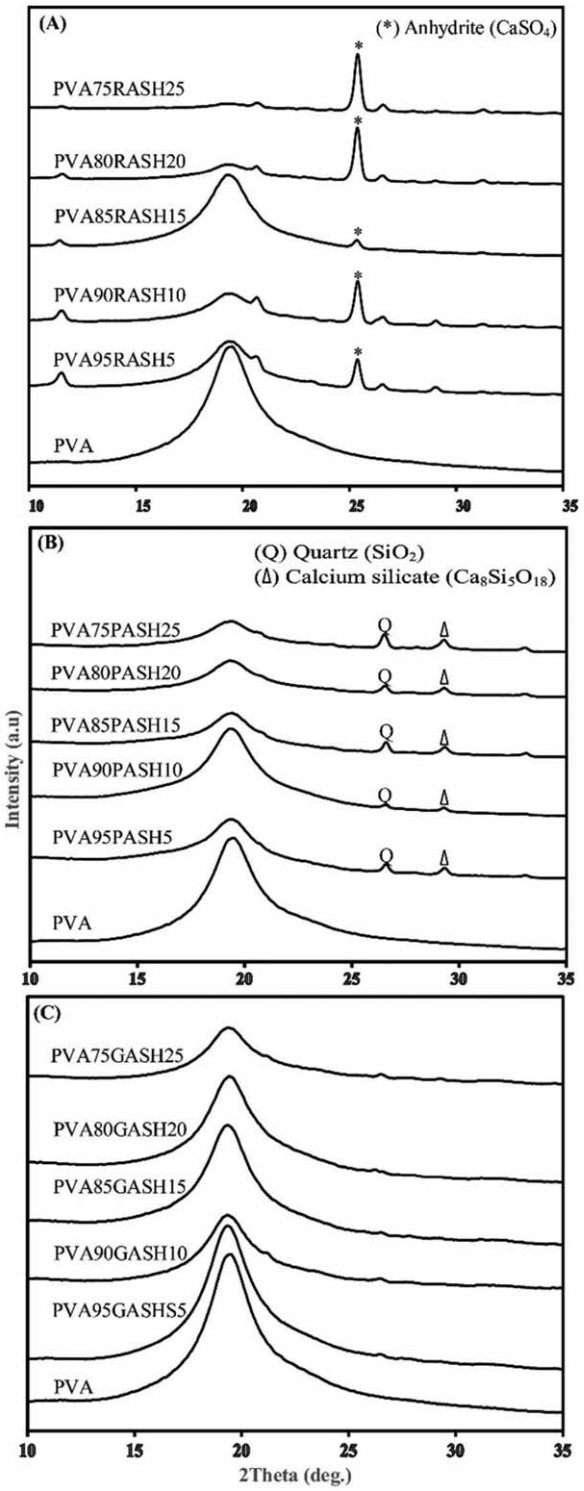

Figure 9. XRD patterns of (A) PVA and PVA/RASH composites, (B) PVA and PVA/PASH composites; (C) PVA and PVA/GASH composites. (*) Anhydrite ($CaSO_4$), (Q) quartz (SiO_2), (Δ) calcium silicate ($Ca_8Si_5O_{18}$).

matrix on the surface of PASH particles. A few interfacial voids with bridge-like connection were seen in Figure 11(C), while these voids were more abundant in Figure 11(D) when PASH loading increased to 25%, which was able to explain brittle failure and poor filler–matrix adhesion. It is noted that many randomly oriented PASH particles are subjected to tensile stress, which were acting perpendicular to the plane and as a result, the crack propagation occurred parallel to the plane.[25,43,44]

Table V. Crystallite Size of PVA, PVA/RASH, PVA/PASH, and PVA/GASH Composites by XRD Analysis

Sample	2Theta (deg.)	β (deg.)	Crystallite size (Å)
PVA100	19.4	1.01	83.6
PVA95RASH5	19.4	0.99	84.6
PVA90RASH10	19.3	0.97	86.5
PVA85RASH15	19.3	0.99	84.2
PVA80RASH20	19.4	0.98	85.6
PVA75RASH25	19.4	1.00	83.6
PVA95PASH5	19.4	1.00	84.6
PVA90PASH10	19.3	1.00	84.2
PVA85PASH15	19.5	0.99	85.5
PVA80PASH20	19.3	0.99	85.4
PVA75PASH25	19.5	0.97	86.9
PVA95GASH5	19.3	1.00	84.5
PVA90GASH10	19.3	0.97	86.5
PVA85GASH15	19.3	1.00	84.3
PVA80GASH20	19.4	0.98	85.6
PVA75GASH25	19.4	1.01	83.7

Figure 11(E,F) indicates the morphological behaviors of PVA/GASH composites at loading 5 and 25%. Compared with Figure 11(C–F) shows better polymer–filler adhesion. Compared to PVA/PASH composites, the enhanced mechanical performance

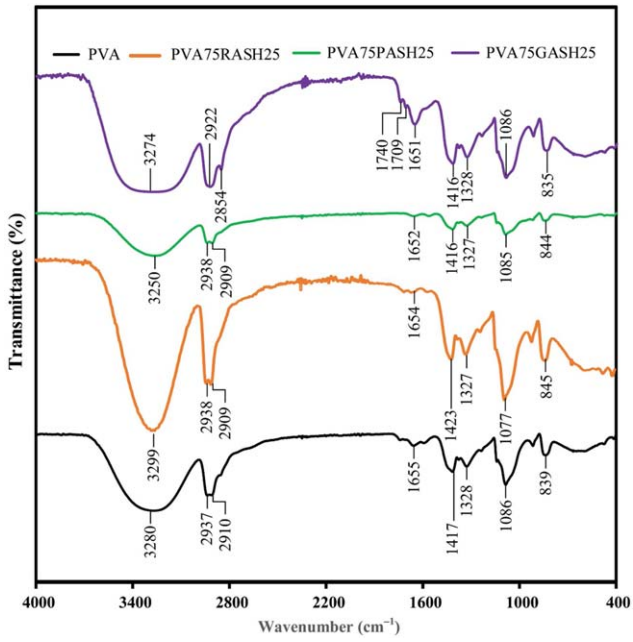

Figure 10. FT-IR spectra of neat PVA, PVA75RASH25, PVA75PASH25, and PVA75GASH25 composites. [Color figure can be viewed in the online issue, which is available at wileyonlinelibrary.com.]

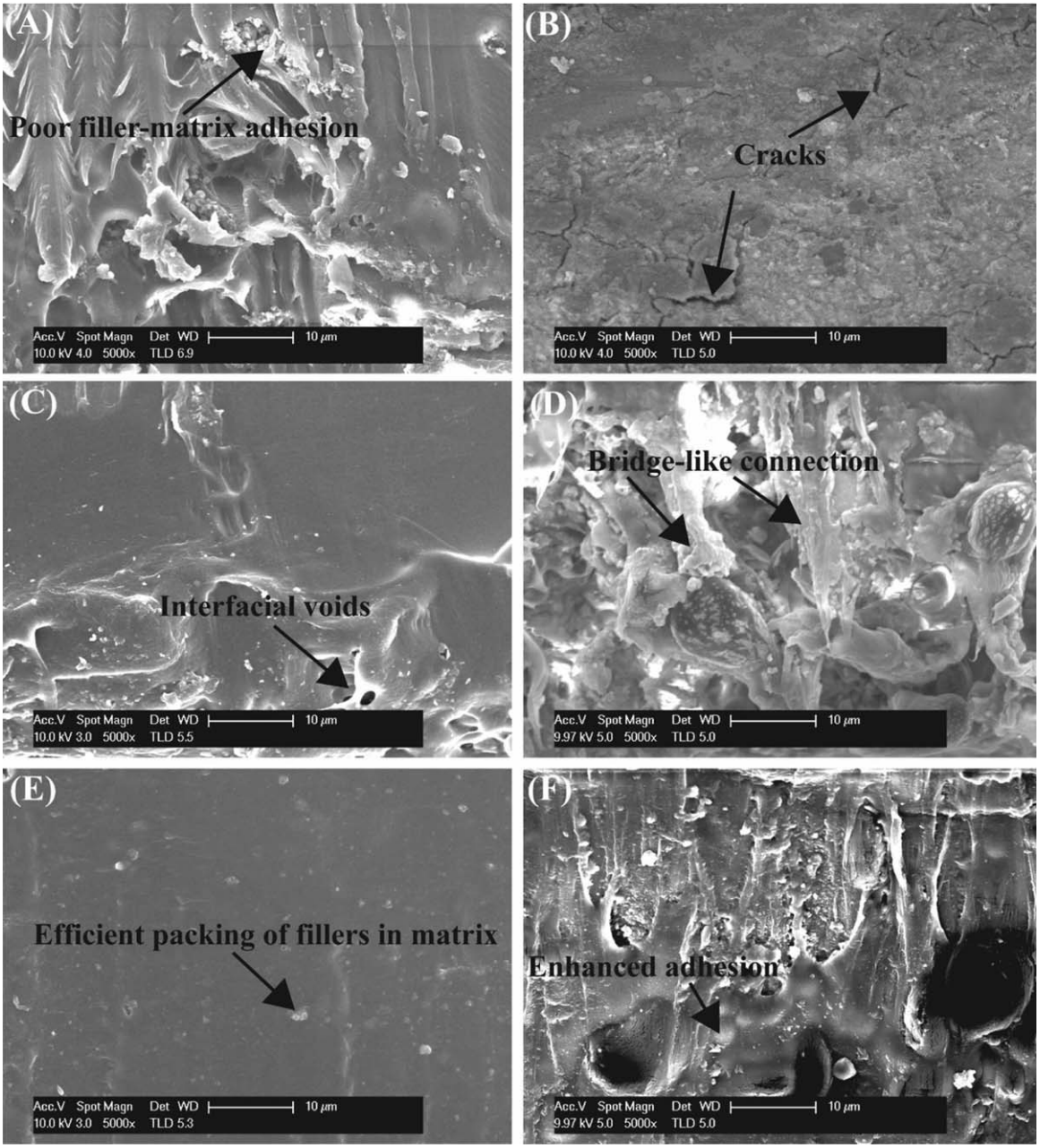

Figure 11. SEM images of fractured cross section composite films: (A) PVA95RASH5 (×5,000); (B) PVA75RASH25 composite (×5,000); PVA95PASH5 composite (×5,000); (B) PVA75PASH25 composite (×5,000); (C) PVA95GASH5 composite (×5,000); (D) PVA75GASH 25 composite (×5,000).

of PVA/GASH attributes to the uniform distribution and efficient packing of GASH in PVA matrix. This is mainly contributed by anchored APTES with $-NH_2$ groups, on the surface of GASH. This anchored APTES makes the surface have highly accessible affinity to the hydrophilic PVA matrix, which contains —OH groups within it. There are almost no interstitial voids in PVA95GASH5 composite and very little in PVA75GASH25 composite. In the absence of interfacial voids, PVA biocomposites tend to have much less local stress, which is mainly responsible for crack initiation, propagation, and finally facture failure.[26] In comparison with the neat polymer matrix, the unique interconnectivity of PVA biocomposites strongly regulates mobility of the segmental chains of polymer, which results in lower elongation behavior.[45] Thus, the composite materials show high tensile strength and lower elongation.[26]

CONCLUSIONS

Microalgal ash, a leftover generated via gasification of the *Nannochloropsis salina* strain was successfully incorporated into polymeric PVA matrix to fabricate biocomposite materials. Hydrothermal-chemical treatment notably improved dispersion and adhesion of PASH within PVA matrix when compared to the RASH. In addition, grafting APTES on the surface of PASH further enhanced interfacial interaction between GASH and PVA matrix, due to strengthening of hydrogen bonding between

—OH groups in PVA and —NH_2 groups on the GASH. Mechanical properties of these biocomposites were in the order of PVA/GASH > PVA/PASH > PVA/RASH, while thermal properties of those are stable. Overall, our developed synthesis process was demonstrated to be efficient, due to activation and surface modification of microalgal ash, and composite fabrication are easily operable. Therefore, microalgae-derived ash can be integrated to downstream processing of microalgal biorefinery, while the total operating cost of microalgal-based facility can be reduced by producing value-added byproduct ashes.

ACKNOWLEDGMENTS

This research was supported by the Advanced Biomass R&D Center (ABC) of Korea Grant funded by the Ministry of Science, ICT and Future Planning (ABC-2010-0029728). We appreciate William I. Suh for helping us to improve writing of this manuscript.

REFERENCES

1. Hirano, A.; Hon-Nami, K.; Kunito, S.; Hada, M.; Ogushi, Y. *Catal. Today* **1998**, *45*, 399.
2. Brandenberger, M.; Matzenberger, J.; Vogel, F.; Ludwig, C. *Biomass Bioenergy* **2013**, *51*, 26.
3. Lee, Y. K. *J. Appl. Phycol.* **1997**, *9*, 403.
4. Nath, D. C. D.; Bandyopadhyay, S.; Boughton, P.; Yu, A.; Blackburn, D.; White, C. *J. Appl. Polym. Sci.* **2010**, *117*, 114.
5. Guhanathan, S.; Saroja Devi, M. *Compos. Interfaces* **2004**, *11*, 43.
6. Gupta, N.; Singh Brar, B.; Woldesenbet, E. *Bull. Mater. Sci.* **2001**, *24*, 219.
7. Wong, K. W. Y.; Truss, R. W. *Compos. Sci. Technol.* **1994**, *52*, 361.
8. Satapathy, S.; Nando, G. B.; Nag, A.; Raju, K. V. S. N. *J. Appl. Polym. Sci.* **2013**, *130*, 4558.
9. Tokiwa, Y.; Calabia, B. P.; Ugwu, C. U.; Aiba, S. *Int. J. Mol. Sci.* **2009**, *10*, 3722.
10. Chung, Y. S.; Kang, S. I.; Kwon, O. W.; Shin, D. S.; Lee, S. G.; Shin, E. J.; Min, B. G.; Bae, H. J.; Han, S. S.; Jeon, H. Y.; Noh, S. K.; Lyoo, W. S. *J. Appl. Polym. Sci* **2007**, *106*, 3423.
11. Fu, C.; Gu, L. *J. Appl. Polym. Sci.* **2013**, *128*, 1044.
12. Qi, Y. Y.; Tai, Z. X.; Sun, D. F.; Chen, J. T.; Ma, H. B.; Yan, X. B.; Liu, B.; Xue, Q. J. *J. Appl. Polym. Sci.* **2013**, *127*, 1885.
13. Huang, C.-L.; Peng, S.-Y.; Wang, Y.-J.; Chen, W.-C.; Lin, J.-H. *J. Appl. Polym. Sci.* **2015**, *132*, DOI: 10.1002/app.41891.
14. Phuchaduek, W.; Jamnongkan, T.; Rattanasak, U.; Boonsang, S.; Kaewpirom, S. *J. Appl. Polym. Sci.* **2015**, *132*, DOI: 10.1002/app.42234.
15. Li, Y.; Tian, H.; Jia, Q.; Niu, P.; Xiang, A.; Liu, D.; Qin, Y. *J. Appl. Polym. Sci.* **2015**, *132*, DOI: 10.1002/app.42706.
16. Chiellini, E.; Cinelli, P.; Imam, S. H.; Mao, L. *Biomacromolecules* **2001**, *2*, 1029.
17. Chiellini, E.; Cinelli, P.; Ilieva, V. I.; Martera, M. *Biomacromolecules* **2008**, *9*, 1007.
18. Peng, J.; Ellingham, T.; Sabo, R.; Clemons, C. M.; Turng, L. S. *J. Appl. Polym. Sci.* **2015**, *132*. DOI: 10.1002/app.42283.
19. Kamoun, E. A.; Chen, X.; Mohy Eldin, M. S.; Kenawy, E.-R. S. **2015**, *8*, 1.
20. Baker, M. I.; Walsh, S. P.; Schwartz, Z.; Boyan, B. D. *J. Biomed. Mater. Res. B: Appl. Biomater.* **2012**, *100*, 1451.
21. Imam, S. H.; Cinelli, P.; Gordon, S. H.; Chiellini, E. *J. Polym. Environ.* **2005**, *13*, 47.
22. Tan, B. K.; Ching, Y. C.; Gan, S. N.; Ramesh, S.; Rahman, M. R. *Mater. Res. Innovat.* **2014**, *18*, S6144.
23. Huang, H.; Gu, L.; Ozaki, Y. *Polymer* **2006**, *47*, 3935.
24. Nath, D. C. D.; Bandyopadhyay, S.; Yu, A.; Blackburn, D.; White, C. *J. Mater. Sci.* **2009**, *45*, 1354.
25. Patil, A. G.; Selvakumar, M.; Anandhan, S. *J. Thermoplast. Compos. Mater.* **2014**, *27*, 1.
26. Nath, D. C. D. *Int. J. Polym. Mater.* **2011**, *60*, 852.
27. Guo, Z.; Zhang, D.; Wei, S.; Wang, Z.; Karki, A. B.; Li, Y.; Bernazzani, P.; Young, D. P.; Gomes, J. A.; Cocke, D. L.; Ho, T. C. *J. Nanopart. Res.* **2009**, *12*, 2415.
28. El-Zaher, N. A.; Osiris, W. G. *J. Appl. Polym. Sci.* **2005**, *96*, 1914.
29. Saroj, A. L.; Singh, R. K. *J. Phys. Chem. Solids* **2012**, *73*, 162.
30. Kaczmarek, H.; Podgórski, A. *J. Photochem. Photobiol. A* **2007**, *191*, 209.
31. Jha, B.; Koshy, N.; Singh, D. N. *Front. Environ. Sci. Eng.* **2014**, *9*, 221.
32. Lee, W. K. W.; van Deventer, J. S. *J. Colloids Surf. A* **2002**, *211*, 49.
33. Palomo, A.; Grutzeck, M. W.; Blanco, M. T. *Cem. Concr. Res.* **1999**, *29*, 1323.
34. Chang, A. C. C.; Chuang, S. S. C.; Gray, M.; Soong, Y. *Energy Fuels* **2003**, *17*, 468.
35. Yamaura, M.; Camilo, R. L.; Sampaio, L. C.; Macêdo, M. A.; Nakamura, M.; Toma, H. E. *J. Magn. Magn. Mater.* **2004**, *279*, 210.
36. George, J. J.; Bhowmick, A. K. *J. Mater. Sci.* **2007**, *43*, 702.
37. Tjong, S. C. *Mater. Sci. Eng. Rep* **2006**, *53*, 73.
38. Kader, M. A.; Kim, K.; Lee, Y. S.; Nah, C. *J. Mater. Sci.* **2006**, *41*, 7341.
39. Agrawal, S. L.; Awadhia, A. *Bull. Mater. Sci.* **2004**, *27*, 523.
40. Kim, G. M.; Asran, A.; Michler, G. H.; Simon, P.; Kim, J. S. *Bioinspir. Biomim.* **2008**, *3*, 046003.
41. Wu, J.; Wang, N.; Wang, L.; Dong, H.; Zhao, Y.; Jiang, L. *Soft Matter.* **2012**, *8*, 5996.
42. Weichold, O.; Möller, M. *Adv. Eng. Mater.* **2007**, *9*, 712.
43. Deepthi, M. V.; Sharma, M.; Sailaja, R. R. N.; Anantha, P.; Sampathkumaran, P.; Seetharamu, S. *Mater. Des.* **2010**, *31*, 2051.
44. Ramos, V. D.; da Costa, H. M.; Soares, V. L. P.; Nascimento, R. S. V. *Polym. Test.* **2005**, *24*, 219.
45. Leong, Y. W.; Abu Bakar, M. B.; Ishak, Z. A. M.; Ariffin, A.; Pukanszky, B. *J. Appl. Polym. Sci.* **2004**, *91*, 3315.